IEEE Access
Multidisciplinary | Rapid Review | Open Access Journal

Received June 4, 2020, accepted July 1, 2020, date of publication July 8, 2020, date of current version July 21, 2020.

Digital Object Identifier 10.1109/ACCESS.2020.3008006

A Unified Anisotropic Particle-Based Ocean Wave Simulation Framework for Marine Simulator Visual System

HAIJIANG LI, HONGXIANG REN, CHANG WANG, AND SHAOYANG QIU
Navigation College, Dalian Maritime University, Dalian 116026, China

Corresponding author: Hongxiang Ren (rhx_dmu@163.com)

This work was supported in part by the National Natural Science Foundation of China under Grant 51679024, and in part by the Fundamental Research Funds for the Central Universities under Grant 3132020372 and Grant 3132020131.

ABSTRACT It is urgent to improve the physical reality of ocean scenes in marine simulator for the maritime industry. In this paper, we propose a unified anisotropic particle-based ocean wave simulation framework for marine simulator. In the unified framework, a novel hybrid SPH method is applied to model the ocean waves, which combines a series of nonlinear density constraints and divergence-free velocity field constraints. By solving density constraints, the particle position distribution is directly adjusted to keep a constant density. Experiments show that the hybrid SPH method has advantages in compressibility and stability. Moreover, a novel stochastic fluctuating wind field model is integrated into the hybrid SPH method. The Perlin noise and a modified log wind profile are introduced to enrich the details of wind field. We also introduce a novel oil spill model for marine simulator based on number density, which can achieve a desired sharp density changes at interfaces between multiple fluids. For real-time surface reconstruction, we propose an improved anisotropic particle transformation method based on the distribution of the neighboring particles. The problem of particle deformation near the boundary is solved by our piecewise correction function, with the sharp features and anisotropy maintained. When calculating the covariance matrix and weighted position, the contribution of neighboring particles in other fluid phases is considered to eliminate gaps between multiple fluids in the oil spill scenes. The simulation results show that our unified anisotropic framework based on the SPH concept can easily integrate other models, has strong expansibility, and is very applicable to simulate complex ocean scenes.

INDEX TERMS Marine simulator, SPH, ocean wave, wind field, oil spill, anisotropic transformation.

I. INTRODUCTION

Particle-based ocean wave simulation is one of the most challenging research topics in computer graphics. The realistic simulation of the dynamic evolution of ocean wave has great applications in the fields such as defense industry, transportation safety training, disaster prevention and preparedness, search and rescue training, game development, film special effects and computer animation. The visual system of marine simulator is one of the important applications of ocean wave simulation. In navigation and maritime science, marine simulator has been widely applied to fields of maritime education and training, marine engineering technology demonstration, navigational safety risk assessment, marine scientific research, etc. The visual system of marine simulator provides virtual scenes of actual training tasks or experiment scenes for the operators, which belongs to the typical dynamic environment modeling and simulation in virtual reality technology. The virtual scenes displayed by the visual system mainly includes ocean waves, lands, target ships, navigation aids, lighthouses, etc. Among them, the ocean wave scenes account for more than half of the entire visual system. Therefore, realistic ocean wave simulation can improve the performance of the marine simulator to meet the urgent demand of the transportation industry.

In the current research of marine simulator, a more prominent problem is the physical reality of the simulated scenes. Most of the ocean wave models applied in marine simulator

The associate editor coordinating the review of this manuscript and approving it for publication was Xiaogang Jin.

are statistical models. Although they have high visual realism, they lack physical basis and have poor expansibility. In addition, the main disadvantage of these grid-based methods is that there may be certain limitations in simulating wave breaking, overturning, fluid-rigid coupling, oil spill, etc. With the improvement of the computing powers of current CPUs and GPUs, some Lagrangian methods in the field of computational fluid dynamics (CFD) have gradually become popular in computer graphics for ocean wave simulation. Meshless Lagrangian approaches, such as Smoothed Particle Hydrodynamics (SPH), are very suitable for simulating free surface fluids. SPH does not need to generate grid in the problem domain, so compared with the grid-based methods, it is more applicable to deal with large deformation problems. SPH method is a particle-based discretization of Navier-Stokes equations (NSE). Therefore, introducing the SPH method into the marine simulator for simulating the ocean scenes can greatly improve the physical reality of the visual system. The ocean wave simulation with high believability can bring the simulator into full play in the field of marine science.

However, SPH also has some limitations. The incompressibility of fluids based on SPH has always been a hot issue of research in fluid simulation for computer graphics. In order to enforce incompressibility, the pressure Poisson equation (PPE) or the equation of state (EOS) will usually require to be solved iteratively, which is time-consuming. In addition, it is also a challenging task to reconstruct a smooth liquid surface from irregularly distributed fluid particles in real time. Although some solutions with good performance have been proposed for the above issues, there is still a lot of room for improvement. Therefore, in order to further improve the performance of the algorithm and provide an effective solution for the physics-based complex ocean wave scenes in marine simulator visual system, in this paper, we propose a unified anisotropic particle-based simulation framework for common ocean wave scenes. The detailed contributions are as follows:

In order to enforce incompressibility, we propose a novel hybrid SPH framework to discretize the governing equations of ocean waves. The hybrid SPH framework combines a series of nonlinear density constraints and divergence-free velocity field constraints, which accelerates the convergence of the method and allows larger time steps. The nonlinear density constraints are the application of Position Based Dynamics (PBD) in fluid simulation. By solving density constraints, the particle position distribution is directly adjusted to keep a constant density. Therefore, our hybrid SPH method inherits the stability and efficiency of the PBD framework.

Usually, wind field models considering air particles are expensive and may have stability problems. Instead of sampling expensive air particles, we propose a novel three-dimensional stochastic fluctuating wind field model based on Perlin noise. The pseudo-random disturbance based on Perlin noise enriches the details of wind wave scene. We simulated the attenuation of wind speed in the vertical direction based on a modified log wind profile. In addition, a fluctuating wind field framework is introduced to flexibly control the period and intensity of the wind field. We apply the wind field to fluid particles in the way we treat gravity, so it can be easily integrated into our hybrid SPH framework.

The physical reality of oil spill scene based on empirical geometry models is insufficient. In this paper, we introduce a novel oil spill model for marine simulator based on number density, which can handle density discontinuities at interfaces between oil and ocean correctly. Instead of standard density interpolation, the novel oil spill model estimates density by measuring the particle density. Moreover, our oil spill model can realistically simulate the oil spill process, including the drift, diffusion, and breakage of the oil slick, and is characterized by high stability and strong expansibility.

For real-time surface reconstruction, we propose an improved anisotropic particle rendering framework. Based on the distribution of the neighboring particles, we adopt the weighted version Principal Component Analysis (WPCA) and singular value decomposition (SVD) to generate an anisotropic transformation matrix for each particle. In the oil spill scenario, we comprehensively considered the contribution of different fluid particles and resolved the issue of overlap and gap at the interface of different fluids. The anisotropic particle framework maintains sharper features in the splashing area, and provides a better solution for smooth screen space fluid surface rendering.

II. RELATED WORK

In marine simulator, ocean waves are mainly simulated by spectrum-based approaches, also known as Fourier domain approaches. In spectrum-based approaches, ocean waves are considered to be composed of an infinite number of individual waves with different amplitudes, different frequencies, different directions, and random phases. Tessendorf [1] proposed an ocean wave simulation framework using spectrum-based approach, which is still used as the main solution of ocean wave simulation in industry until now. Subsequently, according to different simulation scenarios, researchers introduced many different wave spectrums, such as Phillips spectrum [1], Pierson-Moskowitz (PM) spectrum [2], Joint North Sea Wave Observation Project (JONSWAP) spectrum [2], [3], and Texel-Marsen-Arsloe (TMA) spectrum [4], [5]. Spectrum-based approaches are characterized by their rapidity, and are applicable to real-time simulation of large-scale ocean waves. However, most of the existing ocean wave spectrums are semi-empirical and semi-theoretical, and are obtained by means of observation techniques and spectral analysis methods. Compared with physics-based methods, spectrum-based approaches cannot fundamentally reveal the complexity of the ocean wave motion, so their expansibility is poor. Moreover, the generation of height field mesh in the problem domain is a prerequisite for spectrum-based approaches [6], [7], which makes them inapplicable to simulate large deformation scenarios such as wave breaking and splashing.

Due to the above limitations of spectrum-based approaches, researchers tried to use physics-based meshfree methods to simulate ocean waves, such as SPH [8], PBF (Position Based Fluids) [9], and MPS (Moving-Particle Semi-implicit Method) [10]. The SPH method is widely used to simulate ocean wave scenarios, such as frigate sailing on wavy sea [11], cargo ship sailing on highly agitated ocean [8], interaction between ocean waves and lighthouse [9], interaction between ocean and a fast-rotating propeller [12], and ocean waves with realistic foam effects [13]. Since the SPH method suffers from the compressibility issue, researchers proposed a series of incompressible SPH frameworks. These incompressible frameworks can be classified into three classes: SPH with non-iterative EOS solvers, such as weakly compressible SPH (WCSPH) [14]; SPH with iterative EOS solvers, such as predictive-corrective incompressible SPH (PCISPH) [15]; and SPH with PPE solvers, such as implicit incompressible SPH (IISPH) [8], and divergence-free SPH (DFSPH) [16]. The source items employed in PPEs are mainly density invariance (DI) [8], velocity divergence (VD) [16], [17] and particle shift (PS) [18]. The time step of WCSPH is small due to the fixed stiffness parameter. PCISPH has a larger time step by iteratively solving the stiffness parameter. IISPH adopts a PPE with DI as the source term, which further enhances the incompressibility and allows a larger time step. DFSPH introduces a PPE with VD as the source term to further accelerate the convergence rate, and has become one of the fastest SPH methods at present. PBF [9], [19] is an incompressible framework based on PBD [20]. Its incompressibility performs very well and has strong stability. However, compared with the DFSPH method, PBF has longer calculation time under the same conditions.

Compared with SPH method, spectrum-based approaches have the characteristic of randomness. Ocean waves are commonly caused by wind, whose action is much more complicated than gravity, so ocean waves usually appear strong randomness. The wave spectrums contain wind parameters, such as wind speed and direction [1]. Therefore, spectrum-based approaches are applicable to simulate random waves. As we all know, wind is the flow of gases on a large scale. In the context of SPH, the interaction between air and ocean surface can theoretically be modeled as a multiphase flow problem. However, sampling air particles is expensive, and high-density ratio may cause stability problems. Therefore, drag force models are introduced to approximate the interactions between air and fluid [19], [21]. In addition, the research on the interaction between air and fluid has focused on the problems of surface tension [22] and underestimation of the density of fluid particles at the surface [23]. There is relatively little research on wind field modeling in SPH, and the drag force models are inapplicable to simulate the heavy waves in marine simulator.

The research on offshore oil spill aims to understand and quantify the physical and chemical processes during oil spill [24]. The physical process mainly refers to the motion of oil slicks under the influence of wind, wave and current. The dynamic behavior and fate of oil spilled in the ocean environment are mainly classified into three classes: spreading, drifting and dispersion [25], [26]. Early oil spreading models such as Fay model [27] and Lehr model [28], [29] are mostly empirical models. Although empirical methods are fast and efficient, they have limitations in dealing with the interaction with dynamic objects such as oil fence and oil receiver. Drifting and dispersion are the movement of spilled oil under the action of external environmental dynamics, such as ocean surface wind field and flow field. Hoult drifting model [30] and particle-based model [31] are commonly used drifting and dispersion models in marine simulator. However, it is insufficient to describe the dynamic motion of spilled oil based on mathematical models, which tend to have poor expansibility and often require individual modeling for different behaviors. In fact, the oil spill models based on fluid dynamics are ideal methods, such as Finite Differential Method (FDM), Finite Element Method (FEM), and Finite Volume Methods (FVM). But these methods are computationally expensive and cannot be directly applied to marine simulator. However, some popular fluid simulation methods in computer graphics have been successfully introduced into marine simulator, such as NB-FLIP (Narrow Band Fluid Implicit Particle method) [32]–[34]. NB-FLIP is a hybrid method of Lagrangian particles and Eulerian meshes. Combined with the VOF (Volume of Fluid) method, NB-FLIP can flexibly deal with the interaction between spilled oil and obstacles. Compared with the mathematical models, it has strong expandability and broad application prospects. Considering the good performance of SPH method in fluid simulation, SPH method can also be introduced into the simulation of oil spill in marine simulator.

Although the strong expansibility of SPH method is very attractive, the reconstruction of smooth surface is still an inevitable problem. In fact, many methods have been developed to reconstruct smooth surfaces from SPH fluid, such as level set [35], particle level set [36], and marching cubes [37]. If the grid resolution is high enough, these methods can reconstruct the fluid surface with rich details. However, the calculation of signed distance field (SDF) needs to generate grid in the problem domain, which will bring about memory consumption and further affect the efficiency. Van der Laan *et al.* [38] proposed a SPH fluid rendering approach named screen space fluid (SSF), which does not explicitly generate polygonal surface, but renders the fluid surface by smoothing the particle depth map. This fluid rendering method has real-time performance and inherent view-dependent level-of-detail. However, since SSF renders fluid surface directly based on the depth map and thickness map of fluid particles, its surface smoothness needs to be improved. The smoothing methods for depth map mainly include curvature flow [38], bilateral Gaussian filter [39], narrow-range filter [40], etc. But only smoothing the particle depth map cannot completely solve the problem of surface smoothness. Therefore, researchers introduced an anisotropic depth map into SSF [40], [41], which can greatly improve

the surface quality while providing a better preservation of sharp fluid details. This is now one of the best real-time fluid surface rendering algorithms.

III. OCEAN WAVE MODELING

In marine simulator, we assume that the ocean is a homogeneous incompressible fluid with constant temperature and salinity, that is, there is no need to consider the effects of temperature and salinity changes. Therefore, we use the Lagrangian form Navier-Stokes equations as the governing equations of ocean waves:

$$\frac{D\rho}{Dt} + \rho\nabla\cdot\mathbf{v} = 0. \tag{1}$$

$$\rho\frac{D\mathbf{v}}{Dt} = -\nabla p + \mu\nabla^2\mathbf{v} + \mathbf{f}_{ext}. \tag{2}$$

where ρ is the density, t is the time, $\mathbf{v}$ is the velocity, p is the pressure, μ is the dynamic viscosity, and $\mathbf{f}_{ext}$ is the external forces acting on unit fluid element. In order to achieve the randomness of the ocean surface, here, in addition to gravity $\mathbf{g}$, $\mathbf{f}_{ext}$ also includes the stochastic fluctuating wind field we proposed. $\frac{D}{Dt}$ is the substantial derivative.

The relationship between pressure and density can be expressed by the following EOS [16], [42]:

$$p = \kappa\left(\rho - \rho_0\right). \tag{3}$$

where κ is an iteratively solved stiffness coefficient. ρ_0 is the rest density.

A. SPH DISCRETIZATION

In the SPH concept, the fluid in the problem domain is dispersed into a series of fluid particles carrying physical properties. The corresponding physical properties of each fluid particle in (1) and (2) are obtained by interpolation of its neighboring particles.

The SPH approximation for the density ρ_i at position $\mathbf{x}_i$ is given as [43]:

$$\rho_i = \sum\nolimits_j m_j W_{ij}. \tag{4}$$

where m_j is the mass of particle j. W_{ij} is the kernel function similar to the Gaussian function, and $W_{ij} = W\left(\left|x_i - x_j\right|/h\right)$. h is the support radius.

The spatial derivative of field function can be converted into the derivative of the kernel function ∇W_{ij}, so the velocity divergence in the continuity equation can be expressed as [43]:

$$\nabla\cdot\mathbf{v}_i = -\frac{1}{\rho_i}\sum\nolimits_j m_j\mathbf{v}_{ij}\cdot\nabla W_{ij}. \tag{5}$$

where $\nabla W_{ij} = \left(\frac{\partial W_{ij}}{\partial x_{i,x}}, \frac{\partial W_{ij}}{\partial x_{i,y}}, \frac{\partial W_{ij}}{\partial x_{i,z}}\right)^T$, and $\mathbf{v}_{ij} = \mathbf{v}_i - \mathbf{v}_j$.

The viscous term in (2) can be expressed as [45]:

$$\nabla^2\mathbf{v}_i = 2(d+2)\sum\nolimits_j \frac{m_j}{\rho_j}\frac{\mathbf{v}_{ij}\cdot\mathbf{x}_{ij}}{\mathbf{x}_{ij}\cdot\mathbf{x}_{ij} + 0.01h^2}\nabla W_{ij}. \tag{6}$$

where d is the spatial dimension, the term $0.01\ h^2$ is introduced to avoid singularities, and $\mathbf{x}_{ij} = \mathbf{x}_i - \mathbf{x}_j$.

In our hybrid SPH framework, we have adopted a pressure projection scheme. Pressure and non-pressure accelerations are applied separately. Under the action of non-pressure, an intermediate velocity $\mathbf{v}_i^*$ will be predicted first:

$$\mathbf{a}_i^{nonp} = \frac{\mu}{\rho_i}\nabla^2\mathbf{v}_i + \frac{\mathbf{f}_{ext}}{\rho_i}. \tag{7}$$

$$\mathbf{v}_i^* = \mathbf{v}_i(t) + \Delta t\mathbf{a}_i^{nonp}(t) \tag{8}$$

where $\mathbf{a}_i^{nonp}$ is the non-pressure acceleration of particle i. Δt is time step size.

1) DIVERGENCE-FREE VELOCITY FIELD

In the pressure projection scheme, the intermediate velocity $\mathbf{v}_i^*$ is projected into a divergence-free velocity field by pressure:

$$\mathbf{v}(t+\Delta t) = \mathbf{v}_i^* - \frac{\Delta t}{\rho_i}\nabla p_i. \tag{9}$$

where $\nabla\cdot\mathbf{v}(t+\Delta t) = \mathbf{0}$. Taking gradients on both sides of (9) at the same time, we get:

$$\nabla^2 p_i = \frac{\rho_i}{\Delta t}\nabla\cdot\mathbf{v}_i^*. \tag{10}$$

Equation (10) is a PPE with velocity divergence as the source term. To solve the PPE (10), the pressure should be calculated based on the pressure gradient. The pressure gradient can be obtained according to the EOS expressed in (3). Taking the derivative of both sides of (3), we will get the pressure gradient for particle i:

$$\nabla p_i = \kappa_i\nabla\rho_i. \tag{11}$$

The pressure gradient can be discretized as [16]:

$$\nabla p_i = \kappa_i\sum\nolimits_j m_j\nabla W_{ij}. \tag{12}$$

According to the momentum equation (2) the pressure force $\mathbf{F}_i^p$ of particle i can be expressed as:

$$\mathbf{F}_i^p = -\frac{m_i}{\rho_i}\nabla p_i = -\frac{m_i}{\rho_i}\kappa_i\sum\nolimits_j m_j\nabla W_{ij}. \tag{13}$$

According to Newton's third law of motion, the particle i exerts a reaction force $\mathbf{F}_{j\leftarrow i}^p$ on the neighboring particles while being subjected to the pressure $\mathbf{F}_i^p$ from the neighboring particles. The value of $\mathbf{F}_{j\leftarrow i}^p$ is equal to the pressure of the corresponding neighboring particle j acting on the particle i, and the direction is opposite:

$$\mathbf{F}_{j\leftarrow i}^p = \frac{m_i}{\rho_i}\kappa_i m_j\nabla W_{ij}. \tag{14}$$

Velocity changes caused by this set of symmetric pressure forces are $\Delta\mathbf{v}_i = \Delta t\frac{\mathbf{F}_i^p}{m_i}$, $\Delta\mathbf{v}_j = \Delta t\frac{\mathbf{F}_{j\leftarrow i}^p}{m_i}$. According to (5), the pressure velocity divergence can be expressed as:

$$\nabla\cdot\left(-\Delta t\frac{1}{\rho_i}\nabla p_i\right) = -\frac{1}{\rho_i}\sum\nolimits_j m_j\Delta\mathbf{v}_{ij}\cdot\nabla W_{ij}. \tag{15}$$

Substituting $\Delta\mathbf{v}_i$ and $\Delta\mathbf{v}_j$ into (13), we can get:

$$\nabla^2 p_i = \frac{1}{m_i}\sum\nolimits_j m_j\left(\mathbf{F}_i^p - \mathbf{F}_{j\leftarrow i}^p\right)\cdot\nabla W_{ij}. \tag{16}$$

Equation (16) is the SPH discrete form of the left side of (10). For the right side of (10), it can be directly discretized according to (5):

$$\frac{\rho_i}{\Delta t}\nabla\cdot\mathbf{v}_i^* = -\frac{1}{\Delta t}\sum\nolimits_j m_j\mathbf{v}_{ij}^*\cdot\nabla W_{ij} = -\frac{1}{\Delta t}\frac{D\rho_i^*}{Dt}. \quad (17)$$

According to (10), (16) and (17), we can obtained:

$$\frac{D\rho_i^*}{Dt} = -\frac{\Delta t}{m_i}\sum\nolimits_j m_j\left(\mathbf{F}_i^p - \mathbf{F}_{j\leftarrow i}^p\right)\cdot\nabla W_{ij}. \quad (18)$$

Substituting (13) and (14) into Equation (18) yields:

$$\kappa_i = \frac{\rho_i}{\Delta t}\frac{D\rho_i^*}{Dt}\alpha_i. \quad (19)$$

where $\alpha_i = \frac{-1}{\left(\left|\sum_j m_j\nabla W_{ij}\right|^2 + \sum_j |m_j\nabla W_{ij}|^2\right)}$. Then the total force of particle i is:

$$\begin{aligned}\mathbf{F}_{i,total}^p &= \mathbf{F}_i^p + \mathbf{F}_{i\leftarrow j}^p \\ &= -m_i\sum\nolimits_j m_j\left(\frac{\kappa_i}{\rho_i} + \frac{\kappa_j}{\rho_j}\right)\nabla W_{ij}. \end{aligned} \quad (20)$$

Divergence-free solver iteratively solves PPE with velocity divergence as its source term, forcing the fluid to satisfy incompressibility based on the continuity equation. But solving PPE is generally considered to be time-consuming for large systems. In DFPSH method proposed by Bender *et al.* [16], [17], after solving the PPE with velocity divergence as source term, the PPE with density deviation as source term is also introduced. This combination of PPEs improves the convergence of the SPH method and achieves the best performance. Considering the stability and good incompressibility of PBF method, we tried another combination, that is, replacing the density deviation in the DFSPH combination with a constraint equation. Fortunately, some parameters in divergence-free solver can be reused in constraint equation, which also facilitates the coupling of the two solvers.

2) POSITION BASED DENSITY CONSTRAINTS

In our hybrid SPH, we try to solve density constraint solver based on PBD [9], [19] to further correct the particle position. The density constraint equation C_i for particle i is a function of the particle's position $\mathbf{x}_i$ and the positions of its neighbors:

$$C_i(\mathbf{x}) = \frac{\rho_i}{\rho_0} - 1 \le 0. \quad (21)$$

where $\mathbf{x} = [\mathbf{x}_1, \ldots, \mathbf{x}_n]$, n is the cardinality.

The density constraint solver we introduced aims to find a position correction $\Delta\mathbf{x}$ to satisfy the following constraints:

$$C(\mathbf{x} + \Delta\mathbf{x}) \le 0. \quad (22)$$

Apply Taylor theorem to (22), and truncate it to first order:

$$C(\mathbf{x} + \Delta\mathbf{x}) \approx C(\mathbf{x}) + \nabla C(\mathbf{x})\cdot\Delta\mathbf{x}. \quad (23)$$

In order to ensure momentum conservation of the system, we limit the direction of the particle correction $\Delta\mathbf{x}$ to the direction of the constraint gradient $\nabla C(\mathbf{x})$:

$$\Delta\mathbf{x} = \lambda\nabla C(\mathbf{x}). \quad (24)$$

Taking the derivative of both sides of (21), we will get the constraint gradient for particle i:

$$\nabla C_i(\mathbf{x}) = \frac{1}{\rho_0}\nabla\rho_i. \quad (25)$$

The right side of (25) can be approximated by the SPH discrete form of the spatial derivative of density:

$$\nabla C_i(\mathbf{x}) = \frac{1}{\rho_0}\sum\nolimits_j m_j\nabla W_{ij}. \quad (26)$$

Similarly, we can obtain a pressure gradient $\nabla C_{j\leftarrow i}(\mathbf{x})$ of a particle i acting on its neighboring particle j according to Newton's third law of motion:

$$\nabla C_{j\leftarrow i}(\mathbf{x}) = -\frac{1}{\rho_0}m_j\nabla W_{ij}. \quad (27)$$

Plugging (24), (26) and (27) into (23) yields:

$$\lambda_i = -\frac{\rho_0^2\, C_i(\mathbf{x})}{\nabla C_i^2(\mathbf{x}) + \nabla C_{i\leftarrow j}^2(\mathbf{x})} = \rho_0^2\alpha_i C_i(\mathbf{x}). \quad (28)$$

where $\nabla C_{i\leftarrow j}(\mathbf{x})$ is the pressure gradient acting on particle i from its neighboring particle j. $\nabla C_{i\leftarrow j}(\mathbf{x})$ and $\nabla C_{j\leftarrow i}(\mathbf{x})$ are equal and opposite.

Plugging (28) into (24), the position correction $\Delta\mathbf{x}_i$ of particle i under the action of density constraint can be obtained:

$$\Delta\mathbf{x}_i = \lambda_i\nabla C_i(\mathbf{x}) + \sum\nolimits_j \lambda_j\nabla C_{i\leftarrow j}(\mathbf{x}). \quad (29)$$

Substituting (26) and $\nabla C_{i\leftarrow j}(\mathbf{x})$ in (29) yields:

$$\Delta\mathbf{x}_i = \frac{1}{\rho_0}\sum\nolimits_j m_j(\lambda_i + \lambda_j)\nabla W_{ij}. \quad (30)$$

Density constraint solver further corrects the particle position according to the density constraint equation, which will improve the incompressibility, on the other hand, will lessen calculative burden of divergence-free solver and accelerate its convergence.

3) STOCHASTIC FLUCTUATING WIND FIELD

In the common SPH models, the external force $\mathbf{f}_{ext}$ usually only includes gravity $\mathbf{g}$. Although this can simulate many common fluid scenes, the motion will be regular when simulating the ocean waves. But we all know that wave motion is random, and wind is one of the most important factors. In addition, wind and waves in marine simulator can be used to train the officer's ship handling skills in heavy wind wave condition, and also be used for engineering demonstrations such as testing the strength of ships, offshore structures, breakwaters and other structures. In SPH framework, we habitually consider sampling the surrounding air, and treating air particles as another fluid particles with different rest density. The existing multiphase flow approaches may be used to simulate the interaction between fluid and the air phase. However, the number of sampled air particles is huge. As the scope of the scene expands, the air particles will greatly increase, which will dramatically increase the computation of SPH model. Moreover, the high-density ratio

between air and fluid can cause stability problems. Therefore, in order to simulate the wind field acting on the ocean in the marine simulator visual system, we propose a novel stochastic fluctuating wind field model. Instead of sampling the surrounding air, we try to add wind velocity directly to the fluid particles. The wind velocity is computed by our stochastic fluctuating wind field in real time.

First, the proposed wind field model gives a reference wind velocity $\mathbf{v}_{i,hori}^{wind}$ at a specific height in the horizontal direction. The horizontal wind velocity $\mathbf{v}_{i,hori}^{wind}$ is mainly set according to Beaufort wind scale. In order to generate a stochastic wind field, we added a stochastic disturbance based on Perlin noise to the horizontal wind field. Perlin noise has a pseudorandom appearance. For the same input, the same random number will be generated. Taking millisecond timestamp as random number seed, a three-dimensional stochastic disturbance wind velocity $\mathbf{v}_{i,stoch}^{wind}$ is generated for particle i:

$$\begin{cases} v_{i,x}^{wind} = f^{perlin}(\mathbf{x}_i, A, tseed), \\ v_{i,y}^{wind} = f^{perlin}(\mathbf{x}_i, A, tseed + 1), \\ v_{i,z}^{wind} = f^{perlin}(\mathbf{x}_i, A, tseed - 1) \end{cases} \tag{31}$$

where $v_{i,x}^{wind}$, $v_{i,y}^{wind}$ and $v_{i,z}^{wind}$ are the components of $\mathbf{v}_{i,stoch}^{wind}$ in the three coordinate axes. f^{perlin} is the Perlin noise function, and $tseed$ is the millisecond timestamp. The noise value generated by the initial Perlin noise is between $[-1, 1]$. In order to facilitate the control of the disturbance amplitude, we introduce an amplitude parameter A.

After stochastic disturbance, a stochastic wind field can be generated:

$$\mathbf{v}_{i,ref}^{wind} = \mathbf{v}_{i,hori}^{wind} + \mathbf{v}_{i,stoch}^{wind}. \tag{32}$$

where $\mathbf{v}_{i,ref}^{wind}$ is the reference wind velocity at a reference height h_{ref} from the bottom of the water, and $h_{ref} = 10m$.

However, in actual scenes, attenuation of wind velocity exits. When the wind acts on the ocean surface, the fluid particles closer to the surface are more affected by the wind, so their speed will be faster. However, due to the effect of viscous forces and other forces, the energy brought by the wind will attenuate with the increase of the depth. Therefore, the wind velocity of the fluid particles will also show a trend of vertical attenuation. In our wind field model, inspired by the log wind profile equation, we modeled the attenuation of wind velocity of ocean particles with depth and adopt a semi-empirical logarithmic form ocean particle velocity attenuation equation:

$$\mathbf{v}_i^{wind} = \beta \frac{\rho_{air}}{\rho_i} \frac{\mathbf{v}_{i*}^{wind}}{\kappa} \ln\left(\frac{z_i}{z_0}\right). \tag{33}$$

where $\mathbf{v}_i^{wind}$ is the wind velocity of ocean particle i. β is a control factor, which is used to control the intensity of the wind field. $\rho_{air} = 1.293\ \mathrm{kg \cdot m^{-3}}$ is the density of the surrounding air. Since the high-density ratio between air and liquid may cause the stability problems, we introduce the density ratio ρ_{air}/ρ_i to the log curve. $\mathbf{v}_{i*}^{wind}$ is the friction velocity, $\kappa = 0.41$ is the Von Kármán constant. z_i is the vertical coordinate value of ocean particle i. $z_0 = 0.01$ is the roughness length of zero plane.

The friction velocity $\mathbf{v}_{i*}^{wind}$ can be computed using the following equation:

$$\mathbf{v}_{i*}^{wind} = \kappa \frac{\mathbf{v}_{i,ref}^{wind}}{\ln\left(h_{ref}/z_0\right)}. \tag{34}$$

We have constructed a three-dimensional stochastic wind field based on Beaufort wind scale, Perlin noise and log attenuation equation. But the action of wind is intermittent, so we should construct a fluctuating wind field. Therefore, we design a periodic and asymmetrical pulse wave function to control the continuity of the wind field:

$$\Delta\mathbf{v}_i^{wind}(t) = \begin{cases} \mathbf{v}_i^{wind}(t), & NT < t < NT + pw \\ 0, & NT + pw < t < (N+1)T \end{cases} \tag{35}$$

where $\Delta\mathbf{v}_i^{wind}(t)$ represents the velocity change caused by the wind field, T is the pulse period, pw is the pulse width, N is the natural number. t denotes the time step or frame. Users can set different pulse periods and widths according to different scenarios and requirements, and flexibly control the action of the proposed wind field.

IV. OIL SPILL SIMULATION

Oil spill is such a disaster which causes huge and widespread damage to marine ecological system. The oil spill simulation in marine simulator can be used to train the officer's emergency handling capabilities in the event of an oil spill. The research on oil spill and ocean waves should be conducted together, but most of the current research is separate, that is, the oil spill model or ocean wave model is studied separately, which will bring serious applicability problems. If the oil spill model and ocean wave model do not couple well, they cannot be applied in the marine simulator. Therefore, based on our hybrid SPH framework, we propose a novel particle-based method for oil spill simulation in marine simulator. Our oil spill model is developed based on the ocean wave model, which is more applicable than other methods.

In the SPH concept, oil spill simulation is a typical multi-phase flow problem. The contribution of particles from other phases should be considered in the estimation of the physical quantities of fluid particles at interfaces between multiple fluids. However, if the particle density is computed using (4), the estimated density at the interface will be too large for lower density phase or insufficient for higher density phase. As shown in Fig. 1, for a more intuitive explanation, we build a one-dimensional SPH framework. The rest densities of the fluid in the blue area and the orange area are $1000\ \mathrm{kg \cdot m^{-3}}$, and $400\ \mathrm{kg \cdot m^{-3}}$, respectively. The blue curve represents the density curve computed by (4). It can be seen that there is a significant error in the density estimation at the interface. In oil spill simulation, this may cause numerical instability. Since the oil slick is a kind of fluid sheets, the entire oil

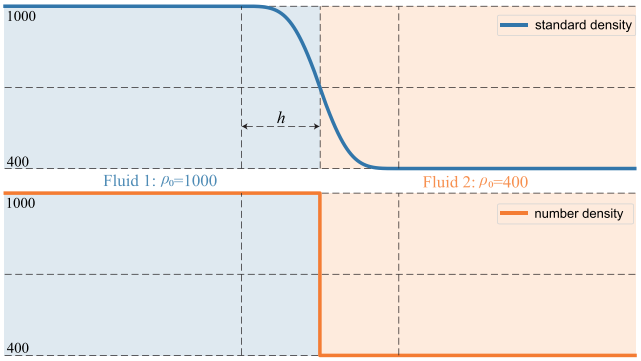

FIGURE 1. A one-dimensional SPH density estimation. The rest density of the fluid in the blue area is 1000 kg · m^{-3}, and the rest density of the fluid in the orange area is 400 kg · m^{-3}. The blue curve is the standard density estimation, and the orange curve is the number density estimation.

slick is almost located on the interface, so the error in density estimation will cause severe distortion in oil spill simulation.

In order to solve the above problems, we introduce a particle number density model to simulate oil spill scenarios. In our unified model, we require constant rest volumes throughout the particles. In the number density model, it is assumed that all particles in the neighborhood of i have the rest density of particle i. Therefore, the improved density of particle i can be expressed as:

$$\tilde{\rho}_i = \rho_{i,0} \sum_k \sum_{j=1}^{N_k} V_j W_{ij}. \tag{36}$$

where $\rho_{i,0}$ is the rest density of the fluid phase containing particle i. k is the index of fluid phase, N_k is the number of neighboring particles in fluid phase k. V_j is the particle volume. The neighboring particles here include not only the fluid particles in the same fluid phase with i, but also the neighboring particles from other fluid phases in the support domain of i. The density curve computed by (36) is shown in the orange curve in Fig. 1. At the interface, it achieves sharp density changes, and the estimation of fluid density is ideal.

Based on the concept of number density, in divergence-free solver and density constraint solver, the estimation of related physical quantities should also be re-derived. The common parameter α_i of the two solvers in the oil spill model can be expressed as:

$$\tilde{\alpha}_i = \frac{1}{\rho_{i,0}^2} \frac{-1}{\left|\sum_k \sum_{j=1}^{N_k} V_j \nabla W_{ij}\right|^2 + \sum_k \sum_{j=1}^{N_k} |V_j \nabla W_{ij}|^2}. \tag{37}$$

The density change rate can be expressed as:

$$\frac{D\tilde{\rho}_i}{Dt} = \rho_{i,0} \sum_k \sum_{j=1}^{N_k} V_j \mathbf{v}_{ij} \cdot \nabla W_{ij}. \tag{38}$$

The new stiffness coefficient $\tilde{\kappa}_i$ for particle i can be expressed as:

$$\tilde{\kappa}_i = \frac{\tilde{\rho}_i}{\Delta t} \frac{D\tilde{\rho}_i}{Dt} \tilde{\alpha}_i. \tag{39}$$

The pressure force in divergence-free solver can be expressed as:

$$\tilde{\mathbf{F}}^p_{i,total} = -m_i \rho_{i,0} \sum_k \sum_{j=1}^{N_k} \left(\frac{\tilde{\kappa}_i}{\tilde{\rho}_i} + \frac{\rho_{j,0}}{\rho_{i,0}} \frac{\tilde{\kappa}_j}{\tilde{\rho}_j} \right) V_j \nabla W_{ij}. \tag{40}$$

The density constraint equation in density constraint solver can be expressed as:

$$\tilde{C}_i(\mathbf{x}) = \frac{\tilde{\rho}_i}{\rho_{i,0}} - 1. \tag{41}$$

The scaling factor λ_i can be expressed as:

$$\tilde{\lambda}_i = \rho_{i,0}^2 \tilde{\alpha}_i \tilde{C}_i(\mathbf{x}). \tag{42}$$

The position correction $\Delta \mathbf{x}_i$ can be expressed as:

$$\Delta \mathbf{x}_i = \sum_k \sum_{j=1}^{N_k} \left(\tilde{\lambda}_i + \frac{\rho_{j,0}}{\rho_{i,0}} \tilde{\lambda}_j \right) V_j \nabla W_{ij}. \tag{43}$$

V. ANISOTROPIC PARTICLE

Among the particle-based fluid surface reconstruction methods, SSF is a very attractive method. Compared with other reconstruction methods, SSF method is more suitable for real-time fluid simulation, such as ocean wave simulation in marine simulator. However, since SSF does not explicitly reconstruct the polygonal surface, it is necessary to improve the smoothness of the fluid surface, not only by smoothing the depth map of the particles. Therefore, we propose an anisotropic particle framework, which is of great significance for improving the smoothness of SSF surface.

Instead of rendering particles as spheres, we render fluid particles as ellipsoids. The anisotropic particle framework adjusts the size and orientation of particles according to the position distribution of neighboring particles in the support domain. If the neighboring particles in the support domain of fluid particle i are sufficient and evenly distributed, then particle i are isotropic when rendered, as the orange particles in Fig. 2. However, if particle i is near the fluid surface, the neighboring particles along the normal direction is less than that along the tangent direction, so when rendering particle i, we shrink the particle sphere along the normal direction, as the blue particles in Fig. 2.

In order to solve the rotation and scaling matrix for particle i from the position distribution, we applied weighted principal component analysis (WPCA) to the positions of neighboring particles. We compute a weighted position $\mathbf{x}_i^w$ according to the distribution of neighboring particles in support domain of particle i:

$$\mathbf{x}_i^w = \frac{\sum_k \sum_{j=1}^{N_k} w_{ij} \mathbf{x}_j}{\sum_k \sum_{j=1}^{N_k} w_{ij}}. \tag{44}$$

where w is an isotropic weight function:

$$w_{ij} = \begin{cases} 1 - \left(|\mathbf{x}_{ij}|/h\right)^3, & \text{if } |\mathbf{x}_{ij}| < h \\ 0, & \text{otherwise} \end{cases} \tag{45}$$

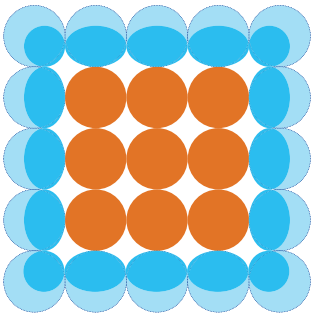

FIGURE 2. 2D schematic diagram of anisotropic particles. Orange particles represent fluid particles with sufficient and evenly distributed neighboring particles, blue particles represent particles near the fluid surface after anisotropic transformation, and light blue particles represent particles near the fluid surface before anisotropic transformation.

Generally speaking, if only the particle distribution inside the single phase is considered, an undesired gap will be generated between the fluids. This is because the particles at the interface between multiple fluids are located on the surface of each fluid phase, so the rendering shape of these particles will be compressed, thereby creating the undesired gap, as shown in Fig. 3a. Therefore, when calculating anisotropic parameters, we consider the contribution of fluid particles from other phases to eliminate the gaps between the fluids, as shown in Fig. 3b.

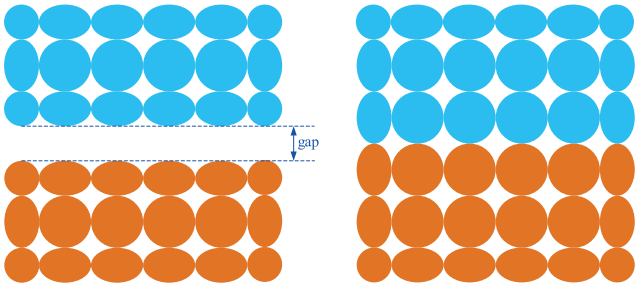

FIGURE 3. A 2D schematic diagram of the gap generated using standard anisotropy method.

The distribution of neighboring particles in the support domain of particle i can be used to construct a weighted covariance matrix $\mathbf{C}_i$:

$$\mathbf{C}_i = \frac{\sum_k \sum_{j=1}^{N_k} w_{ij} \left(\mathbf{x}_j - \mathbf{x}_i^w\right) \left(\mathbf{x}_j - \mathbf{x}_i^w\right)^T}{\sum_k \sum_{j=1}^{N_k} w_{ij}}. \tag{46}$$

Applying singular value decomposition (SVD) to the covariance matrix $\mathbf{C}_i$, the scaling matrix and rotation matrix related to the anisotropic transformation can be obtained:

$$\mathbf{C}_i = \mathbf{R}_i \Sigma_i \mathbf{R}_i^T. \tag{47}$$

where $\mathbf{R}_i$ is the rotation matrix of particle i. Σ_i is a diagonal matrix containing three eigenvalues, and $\Sigma_i = \text{diag}(\sigma_1, \sigma_2, \sigma_3)$, $\sigma_1 \geq \sigma_2 \geq \sigma_3$. Σ_i is the scaling matrix of particle i. Since the particle distribution is arbitrary and noisy, in order to ensure the robustness of SVD, we decompose the covariance matrix $\mathbf{C}_i$ by using the two-sided Jacobi SVD, which is fast and stable for small-scale matrices.

Simulation experiments show that the above rotation and scaling matrix is effective for most particles, and has achieved a good anisotropic transformation effect. However, in areas with only few neighboring particles, the distribution of particles is sparse. Singular value decomposition often produces undesirable results. To solve the problem of particle deformation, Yu and Turk [41] proposed to set a neighboring particle threshold. When the number of neighboring particles is less than the threshold, the particles are set to a unified isotropic value. Although this method effectively solves the problem of particle deformation, it may cause discontinuity or rough boundary details due to improper threshold setting. In the simulation process, we found that among the three eigenvalues obtained by singular value decomposition of the covariance matrix $\mathbf{C}_i$ of particles with few neighboring particles, not all the eigenvalues are abnormal. It is not necessary to reset the correct eigenvalues artificially. While correcting the abnormal eigenvalues, we should maintain the correct eigenvalues as much as possible, so that the particles at the boundary are also anisotropic, and the detailed characteristics of the splashed droplet are retained. Therefore, we propose a novel solution to ensure the continuity of the particle shape and the anisotropic transformation:

$$\tilde{\sigma}_i = \max(\sigma_i, \sigma_1 / k_r). \tag{48}$$

where $k_r = 5.0$ is a scaling factor.

The new scaling matrix can be expressed as:

$$\tilde{\Sigma}_i = \begin{cases} k_s \cdot \text{diag}(\sigma_1, \tilde{\sigma}_2, \tilde{\sigma}_3), & \text{if } N_{nb} \geq N_\epsilon \\ \text{diag}(\xi_1, \xi_2, \xi_3), & \text{if } N_\epsilon > N_{nb} \geq N_t \\ \text{diag}(\zeta_1, \zeta_2, \zeta_3), & \text{if } N_{nb} < N_t \end{cases} \tag{49}$$

where $k_s = 560$ is a scaling factor, $N_\epsilon = 20$ and $N_t = 5$ are threshold constants. ξ_i and ζ_i are improved scaling value in different neighboring particle intervals, and they can be given as:

$$\xi_i = \min\left(1.0, (1-\gamma)k_n + \gamma\tilde{\sigma}_i\right). \tag{50}$$

$$\zeta_i = \min(k_n, \tilde{\sigma}_i). \tag{51}$$

where $k_n = 0.5$ is a scaling factor, and $\gamma \in [0, 1]$, here $\gamma = 0.8$.

Finally, the anisotropic transformation matrix $\mathbf{T}_i$ of particle i can be expressed as:

$$\mathbf{T}_i = \mathbf{R}_i \tilde{\Sigma}_i. \tag{52}$$

After anisotropic transformation, the rendering position of particles will change, especially particles with obvious transformation may cause the problem of particle position noise. Therefore, we should apply on step of Laplacian smoothing on the position of the particles based on the original position $\mathbf{x}_i$ and the weighted position $\mathbf{x}_i^w$:

$$\overline{\mathbf{x}}_i = (1-\tau)\mathbf{x}_i + \tau\mathbf{x}_i^w. \tag{53}$$

where $\tau \in [0, 1]$ is a constant, and here $\tau = 0.9$.

VI. RESULTS AND DISCUSSION

We have implemented the proposed models using C++ in Visual Studio 2019 and built some common ocean scenes to verify the validity of the models. All the simulations were run on a 3.59 GHz AMD Ryzen 7 3700X 8-Core CPU with 32GB of memory. The visualization of particle-based ocean scenes implemented using modern OpenGL and runs on a NVIDIA GeForce RTX 2070 SUPER GPU.

The test ocean scenarios we have built included some fluid-rigid coupling scenarios. All the rigid bodies, including the bounding box were sampled as boundary particles using Poisson Disk Sampling method [46]. The single layer non-uniform boundary particle model [47] is adopted to deal with the two-way coupling between boundary particles and fluid particles. In all test ocean scenarios, the adaptive time step [45] is adopted unless stated otherwise. All length units in the test scenarios are dimensionless, and L is defined as the unit length.

A. PERFORMANCE OF THE HYBRID SPH FRAMEWORK

We built a typical dam break scene to verify the incompressibility of our hybrid SPH framework. In the dam break scene, the size of the bounding box is $5L \times 5L \times 3L$, the size of the fluid block is $1.6L \times 2.0L \times 1.5L$, and the number of fluid particles is 35k. Fig. 4 shows the incompressibility comparison of our hybrid SPH framework and DFSPH framework. In Fig. 4a, the orange curve represents the maximum density value of the hybrid SPH method, and the blue curve represents that of DFSPH method. After introducing position-based density constraints, the stability of the hybrid SPH method is significantly enhanced. Moreover, the DFSPH method has a relatively large peak density fluctuation. Fig. 4b shows the comparison of the average density of the hybrid SPH method and the DFSPH method. The average density level of the hybrid SPH method has steadily increased compared with the DFSPH method. In terms of incompressibility, position based density constraints are more stable than PPE with density invariance as the source term.

Fig. 5 shows the density distribution of the dam break scene simulated by the hybrid SPH method. The rest density of the simulated fluid is 1000 $kg \cdot m^{-3}$. In the area with dense particles, there are sufficient neighboring particles, so the density of the particles is basically at the rest density level. However, the density of particles is relatively low in

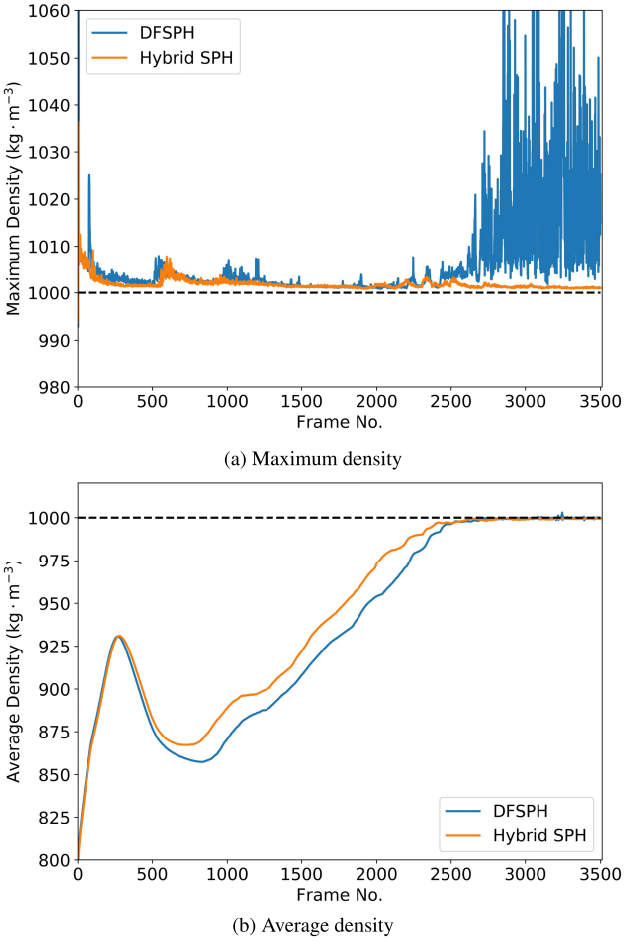

(a) Maximum density

(b) Average density

FIGURE 4. Comparison of incompressibility. Image (a) is the maximum density comparison between our hybrid SPH method and DFSPH method. Image (b) shows the average density comparison.

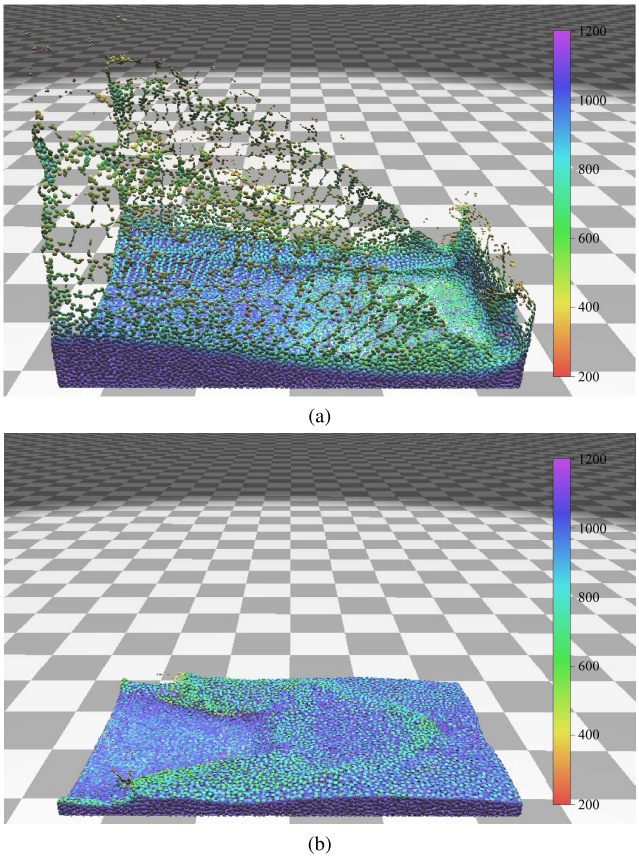

(a)

(b)

FIGURE 5. The density distribution of the dam break scene simulated by the hybrid SPH method. The color bar on the right side of each image describes the density value represented by different colors. The unit of density is $kg \cdot m^{-3}$.

the surface area and splashing area with fewer neighboring particles. This is consistent with the concept of SPH.

Similar to the DFSPH method, in our hybrid SPH method, there are also two solvers, divergence-free solver and density constraint solver (called constant density solver in DFSPH). We separately counted the number of iterations of the two solvers in each method. In the 3500 time steps of the dam break scenario, the average number of iterations of divergence-free solver of both the hybrid SPH method and DFSPH method is 1.0, and the performance is similar. As shown in Fig. 6a, the blue curve represents the number of iterations of the constant density solver of the DFSPH method, and the orange curve represents that of the density constraint solver of the hybrid SPH method. Obviously, the performance of the two methods is similar in the previous time steps. From about the 2500th time step, the convergence of our method is significantly improved. In the 3500 time steps, the average number of iterations of density constraint solver in the hybrid SPH method is 9.3, and that of constant density solver in DFSPH method is 12.0. Since we introduced the density constraint solver from PBF, we compared the number of iterations of the density constraint solver in PBF and hybrid SPH method in Fig. 6b. From Fig. 6b, we can see that our hybrid SPH converges faster in the first 500 time steps.

In Fig. 7, we compared the running time of the solvers. Fig. 7a shows the time costs of divergence-free solvers in DFSPH method and our hybrid SPH method. The time costs of the two methods are almost the same. However, in terms of the time cost of the pressure solvers shown in Fig. 7b, the PBF method, DFSPH method and our hybrid SPH method are quite different. PBF is the most time-consuming among the three methods. The DFSPH method and our hybrid SPH

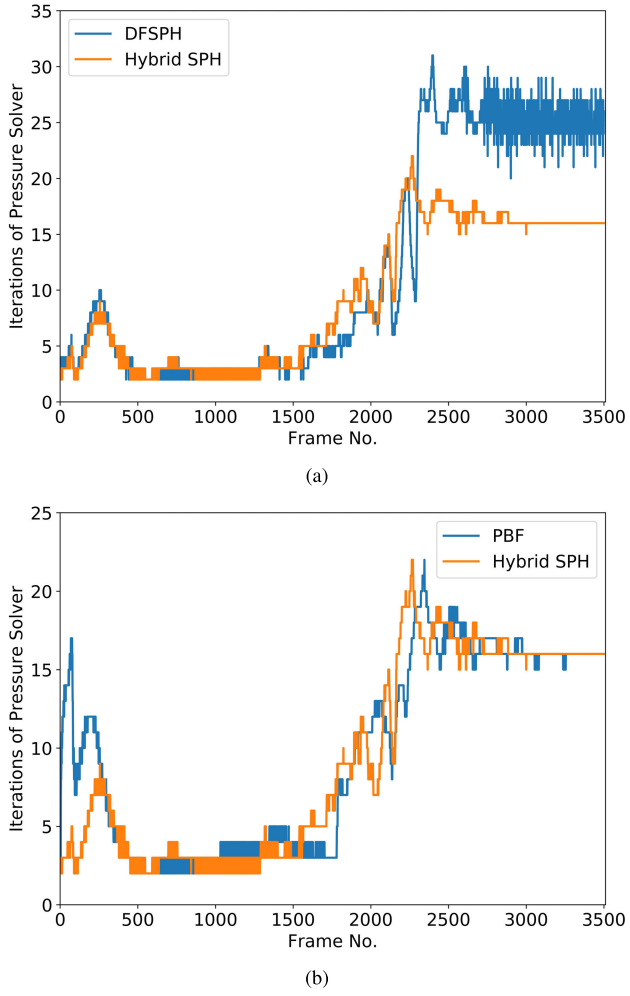

FIGURE 6. Convergence comparison of pressure solvers. Image (a) is the iteration statistics of the density constraint solver in our hybrid SPH method and the constant density solver in DFSPH method. Image (b) is the iteration statistics of the density constraint solver in our hybrid SPH method and PBF method. In order to unify the drawing, in images (a) and (b), we refer to the density constraint solver and the constant density solver as the pressure solver.

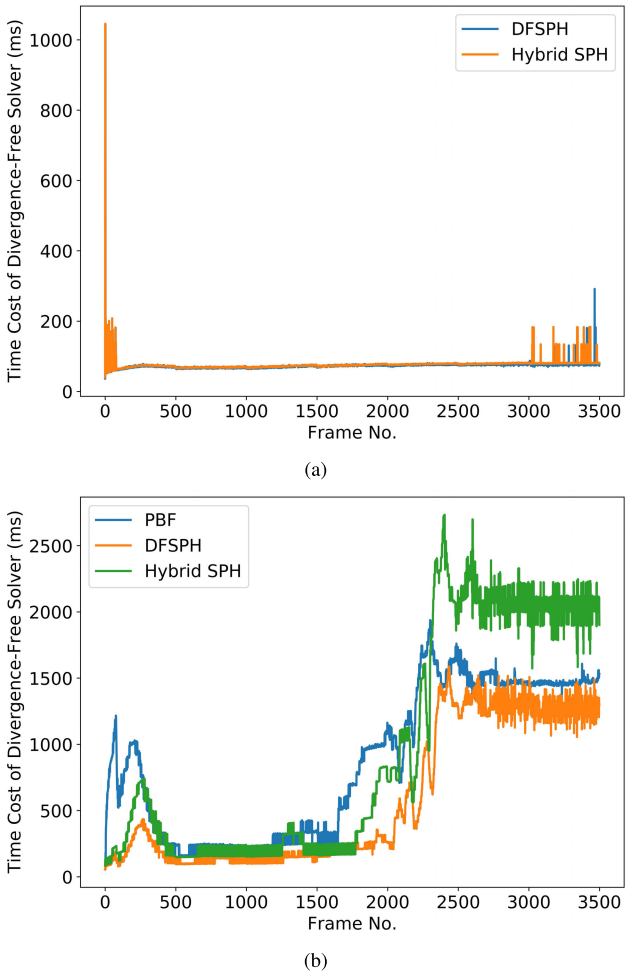

FIGURE 7. Time cost comparison of different solvers. Image (a) is the time cost of the divergence-free solver in our hybrid SPH method and DFSPH method. Image (b) is the time cost of the pressure solvers in our hybrid SPH method, PBF method and DFSPH method. In order to unify the drawing, in image (b), we collectively refer to the density constraint solver and the constant density solver as the pressure solver. The unit of time cost is ms.

method are relatively better. Especially after the 2500th time step, our hybrid SPH method shows more obvious advantage in the rapidness.

B. WIND WAVE SIMULATION

In order to verify the effectiveness of our wind field model, we built some wind wave scenarios. In Fig. 8, the size of the fluid is 5.0L × 0.5L × 2.0L, and the size of the bounding box is 5.0L × 3.0L × 2.0L. The number of fluid particles is 34.7k.

We applied the proposed stochastic fluctuating wind field to the test scene shown in Fig. 8. We use the velocity $\mathbf{v}_{i,hori}^{wind} = (-18, 0, -0.5)$ to initialize the wind field in the horizontal direction. The amplitude A in (31) is set to 3.0, the control factor $\beta = 1.5$, the pulse period $T = 10$, and the pulse width $pw = 100$.We recorded 6000 time steps with a CPU running time of 1.94 h. Fig. 9a shows the meeting scene of two wave peaks, and Fig. 9b shows the scene of wave overturning.

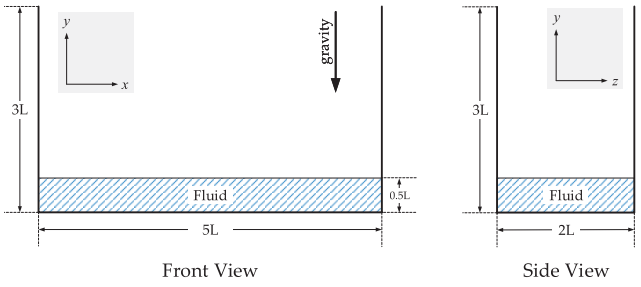

FIGURE 8. General description of the test scene for wind field: front and side views. The black border represents the bounding box. The blue area represents the fluid block.

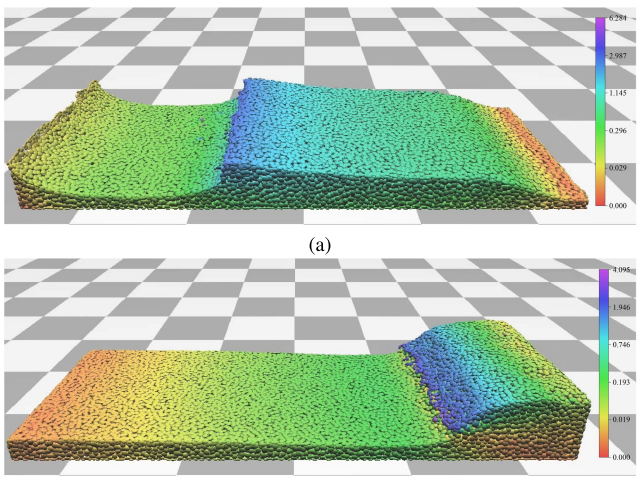

FIGURE 9. Wind field simulation results based on the hybrid SPH framework. The shading of fluid particles is based on their velocity information. The color bars on the right of images (a) and (b) represent the modulus of particle velocity and the unit is m · s^{-1}.

In order to verify the effectiveness of the wind field model in fluid-rigid coupling, we simulated the interaction of wind waves with lighthouse in Fig. 10 and tanker in Fig. 11. In the lighthouse scene, the size of fluid block is

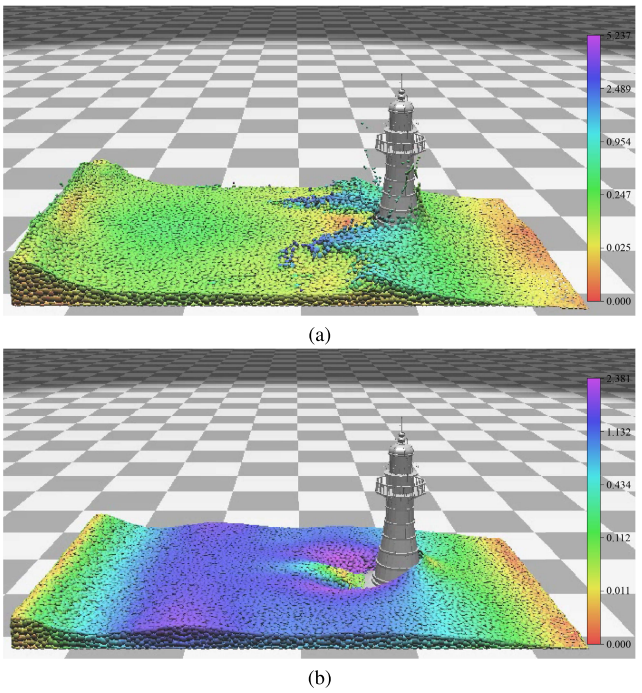

FIGURE 10. Wind waves coupling with a lighthouse. The shading of fluid particles is based on their velocity information. The color bars on the right of images (a) and (b) represent the modulus of particle velocity and the unit is m · s^{-1}.

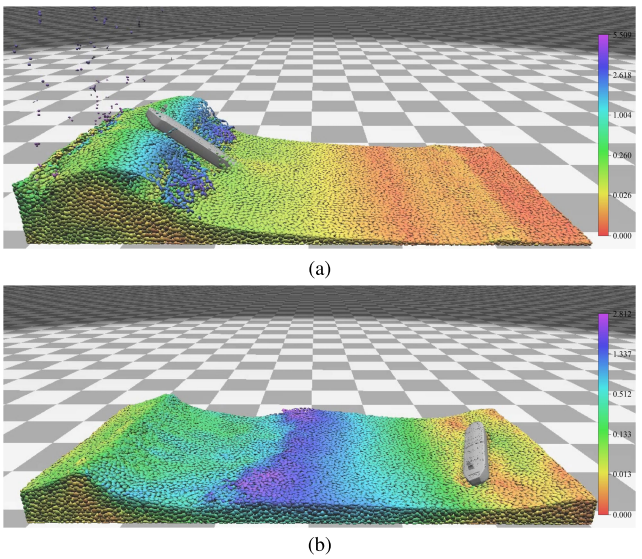

FIGURE 11. A tanker in highly agitated ocean. The shading of fluid particles is based on their velocity information. The color bars on the right of images (a) and (b) represent the modulus of particle velocity and the unit is m · s^{-1}.

3.0L × 0.8L × 2.0L, and the size of the bounding box is 5.0L × 5.0L × 3.0L. The number of fluid particles is 34.5k. The parameters of the wind field applied in Fig. 10 are the same as those in Fig. 9. We recorded 6000 time steps with a CPU running time of 1.17 h. Fig. 10a shows the effect of wind waves hitting the lighthouse.

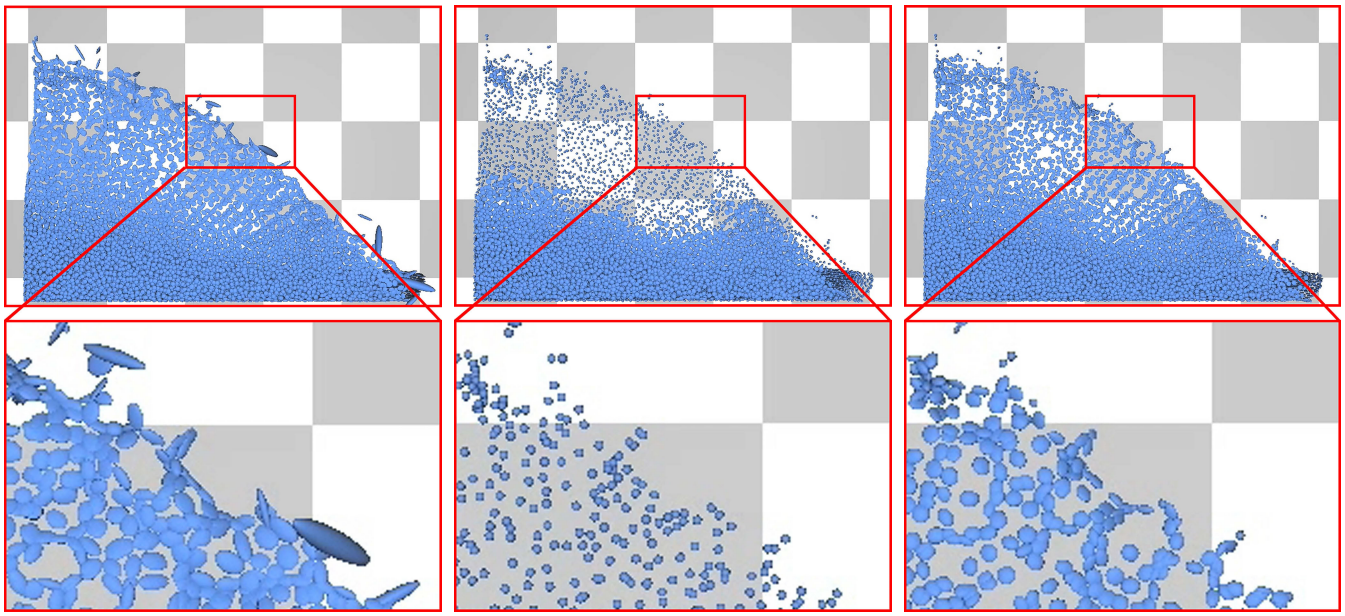

(a) Uncorrected (b) Isotropic Correction (c) Our Method

FIGURE 12. Comparison of abnormal eigenvalue correction methods in anisotropic particle framework. In image (a), the scaling matrix of fluid particles is directly composed of the eigenvalues of SVD. In image (b), when the neighboring particles are less than the threshold, the scaling matrix is artificially set based on Yu's method. In image (c), the abnormal eigenvalues are corrected by our method.

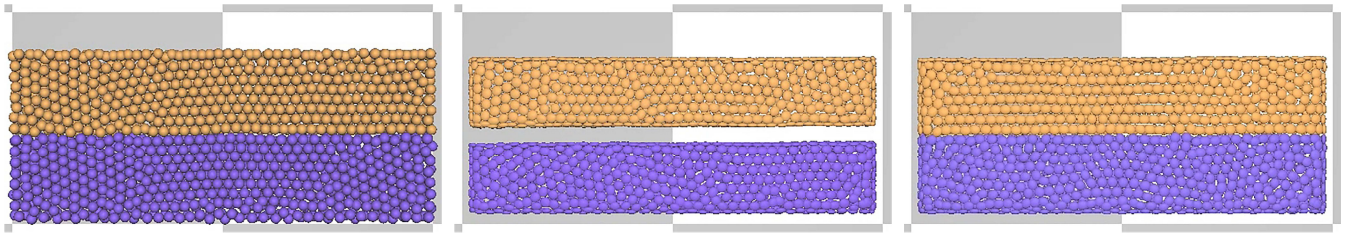

(a) Isotropic particles (b) Anisotropic with gap (c) Anisotropic particles

FIGURE 13. A simple multiphase flow experiment based on the oil spill model. Particles of different colors represent fluids of different rest densities. Image (a) is rendered using isotropic particles. Images (b) and (c) are rendered using isotropic particles. In image (b), the contribution of neighboring particles from other fluid phases is not considered, so there is a gap between different fluids.

The lighthouse in Fig. 10 is a static rigid object. In order to further verify the interaction between wind waves and floating rigid objects, we simulated an oil tanker in highly agitated ocean. As shown in Fig. 11, the size of fluid block is 5.0L × 0.6L × 3.0L, and the size of the bounding box is 6.0L × 5.0L × 3.0L. The number of fluid particles is 64.3k. The parameters of the wind field applied in Fig. 11 are the same as those in Fig. 9 and Fig. 10. We recorded 3000 time steps with a CPU running time of 1.18 h. Fig. 11a shows the effect of the wave overturning under the action of wind and gravity.

C. OIL SPILL AND ANISOTROPIC PARTICLES

Anisotropic transformation is the state-of-the-art method to solve the smoothing problem of particle-based fluid surface. However, if there are insufficient neighboring particles, singular value decomposition will produce abnormal eigenvalues. As shown in Fig. 12a, the particles at the boundary are deformed, and the shape of the splashed particles is generally larger. Yu and Turk proposed an isotropic correction method [41], as shown in Fig. 12b. However, the threshold of neighboring particles and the isotropic value should be carefully selected, otherwise it will cause the discontinuity of the particle shape. After applying our segmented correction method, the size of particles at the boundary is consistent with the particles with sufficient neighboring particles, and the continuity of the particle shape can be better maintained, as shown in Fig. 12c. Moreover, in Fig. 12c, there are some anisotropic particles, which also verifies that our method has kept the anisotropy of particles at the boundary as much as possible.

When dealing with multiphase flow, if the calculation of the anisotropic transformation matrix only considers the contribution of its own neighboring particles, a gap will be generated between different fluid phases, as shown in Fig. 13b. Therefore, when calculating the covariance matrix and weight

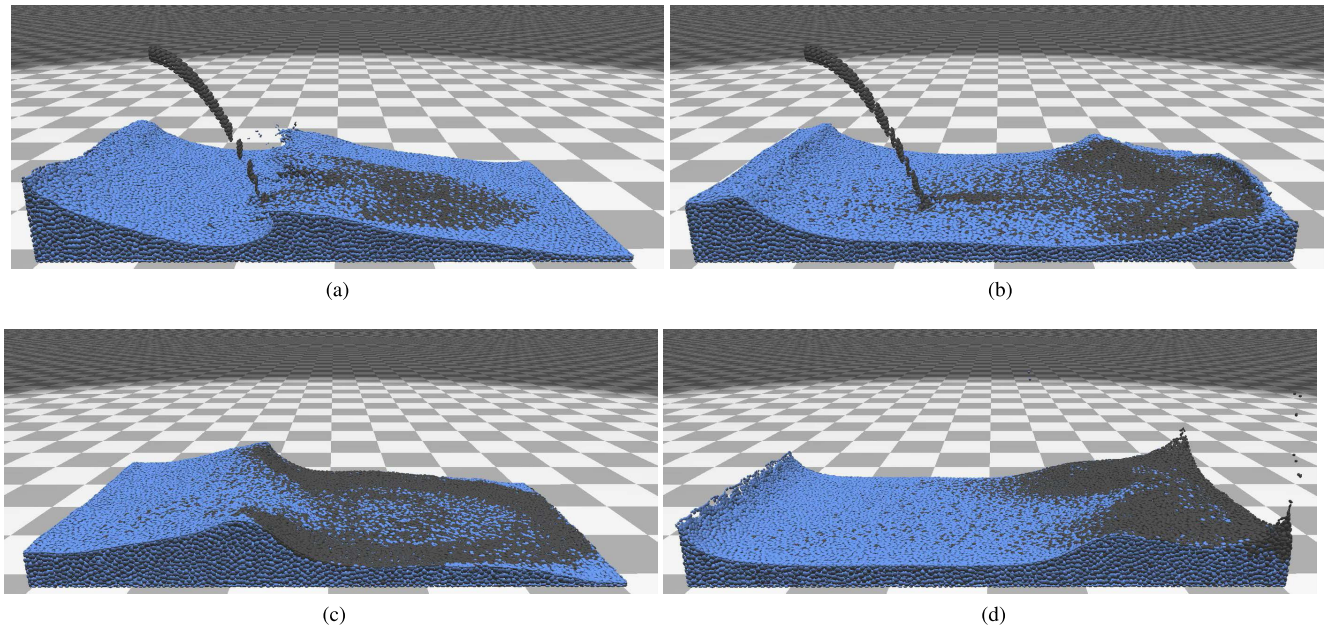

FIGURE 14. Crude oil leaking on the ocean. In images (a) - (d) the rest density of the oil is 800 $kg \cdot m^{-3}$ and that of the ocean is 1027 $kg \cdot m^{-3}$.

positions, we have considered the contribution of neighboring particles in other phases to eliminate the gap between different phase fluids, as shown in Fig. 13c. Compared with the isotropic particles in Fig. 13a, the surface of the anisotropic particles in Fig. 13c is smoother.

We simulated the oil spill based on the anisotropic multiphase flow model. As shown in Fig. 14, the rest density of the oil is 800 $kg \cdot m^{-3}$ and that of the ocean is 1027 $kg \cdot m^{-3}$. The number of ocean particles is 64.3k and that of oil particles is 10k. The parameters of the wind field applied in Fig. 14 are the same as those in Fig. 11. We recorded 9000 time steps with a CPU running time of 6.10 h. In Fig. 14, the oil slick drifts and spreads with the sea water, and sometimes is broken down.

VII. CONCLUSION AND FUTURE WORK

In this paper, we propose a unified anisotropic particle framework for simulating typical marine virtual scenes. The framework is mainly composed of an ocean wave motion model based on hybrid SPH, a stochastic fluctuating wind field based on Perlin noise, and an oil spill model based on particle number density and an anisotropic particle transformation technology. Compared with the spectrum-based approaches, our unified framework is more applicable for simulating large deformation scenes such as splashes. The density constraints from PBD framework are introduced in the hybrid SPH model to further enhance the incompressibility. The stochastic fluctuating wind field model is developed based on the wind profile and Perlin noise, and can be easily integrated into the proposed hybrid SPH model, which is of great significance for the simulation of heavy wind wave scenes in marine simulator. Oil spill simulation based on particle number density solves the problem of inaccurate density estimation at the interfaces between multiple fluids. Compared with the traditional oil spill model, our particle-based oil spill model improves the physical reality of marine oil spill simulation. The improved anisotropic particle method alleviates the discontinuity of the shape of the fluid particles near the boundary, which maintains sharper features and produces a smoother surface. Since the models we proposed are only applicable to virtual reality scenes in marine simulator visual system, similar to most studies on fluid simulation in computer graphics, we prefer to consider stability and rapidity, so we have not compared them with the measured data. Before applying our models to engineering fields such as strength analysis, they need to be compared with the measured data. Some algorithms, such as the time integration scheme, may need to be changed to a higher precision integration scheme. Besides, there are still some areas where our model can be improved. The parameters of the wind field need to be selected carefully. The physical calculation of the unified anisotropic framework is only performed on the CPU, and if applied to the marine simulator, parallel acceleration may be required. In future work, we will continue to optimize the above deficiencies.

REFERENCES

[1] J. Tessendorf, "Simulating ocean water," in *The Elements of Nature: Interactive and Realistic Techniques, ACM SIGGRAPH 2004 Course Notes*. New York, NY, USA: Association for Computing Machinery, Aug. 2004.

[2] C. J. Horvath, "Empirical directional wave spectra for computer graphics," in *Proc. Symp. Digit. Prod. (DigiPro)*, Los Angeles, CA, USA, Aug. 2015, pp. 29–39, doi: 10.1145/2791261.2791267.

[3] J. Fréchot, "Realistic simulation of ocean surface using wave spectra," in *Proc. Int. Conf. Comput. Graph. Theory Appl.*, Setubal, Portugal, Feb. 2006, pp. 76–83.

[4] N. Lee, N. Baek, and K. W. Ryu, "A real-time method for ocean surface simulation using the TMA model," *Int. J. Comput. Inf. Syst. Ind. Manag. Appl.*, vol. 2009, no. 1, pp. 15–21, Dec. 2009.

[5] R. Hopper and K. Wolter, "The water effects of *Pirates of the Caribbean*: Dead men tell no tales," in *Proc. ACM SIGGRAPH Talks (SIGGRAPH)*, Los Angeles, CA, USA, Aug. 2017, pp. 1–2.

[6] D. Hinsinger, F. Neyret, and M.-P. Cani, "Interactive animation of ocean waves," in *Proc. ACM SIGGRAPH/Eurographics Symp. Comput. Animation (SCA)*, San Antonio, TX, USA, Jul. 2002, pp. 161–166, doi: 10.1145/545261.545288.

[7] X. Cui, J. Yi-Cheng, and L. Xiu-Wen, "Real-time ocean wave in multi-channel marine simulator," in *Proc. ACM SIGGRAPH Int. Conf. Virtual Reality Continuum Appl. Ind. (VRCAI)*, Singapore, Jun. 2004, pp. 332–335.

[8] M. Ihmsen, J. Cornelis, B. Solenthaler, C. Horvath, and M. Teschner, "Implicit incompressible SPH," *IEEE Trans. Vis. Comput. Graphics*, vol. 20, no. 3, pp. 426–435, Mar. 2014, doi: 10.1109/TVCG.2013.105.

[9] M. Macklin and M. Müller, "Position based fluids," *ACM Trans. Graph.*, vol. 32, no. 4, pp. 104:1–104:5, Jul. 2013, doi: 10.1145/2461912.2461984.

[10] W. Gou, S. Zhang, and Y. Zheng, "Improvement of pressure calculations in the moving particle semi-implicit method for free-surface flows," *Int. J. Comput. Methods*, to be published, doi: 10.1142/S0219876219500622.

[11] N. Akinci, M. Ihmsen, G. Akinci, B. Solenthaler, and M. Teschner, "Versatile rigid-fluid coupling for incompressible SPH," *ACM Trans. Graph.*, vol. 31, no. 4, pp. 62:1–62:8, Jul. 2012, doi: 10.1145/2185520.2185558.

[12] J. Bender, D. Koschier, T. Kugelstadt, and M. Weiler, "A micropolar material model for turbulent SPH fluids," in *Proc. ACM SIGGRAPH/Eurographics Symp. Comput. Animation*, Los Angeles, CA, USA, Jul. 2017, pp. 4:1–4:8, doi: 10.1145/3099564.3099578.

[13] J. Bender, D. Koschier, T. Kugelstadt, and M. Weiler, "Turbulent micropolar SPH fluids with foam," *IEEE Trans. Vis. Comput. Graph.*, vol. 25, no. 6, pp. 2284–2295, Jun. 2019, doi: 10.1109/TVCG.2018.2832080.

[14] M. Becker and M. Teschner, "Weakly compressible SPH for free surface flows," in *Proc. SCA, ACM SIGGRAPH/Eurographics Symp. Comput. Animation*, San Diego, CA, USA, Aug. 2007, pp. 209–218, doi: 10.2312/SCA/SCA07/209-218.

[15] B. Solenthaler and R. Pajarola, "Predictive-corrective incompressible SPH," *ACM Trans. Graph.*, vol. 28, no. 3, pp. 40:1–40:6, Aug. 2009, doi: 10.1145/1531326.1531346.

[16] J. Bender and D. Koschier, "Divergence-free smoothed particle hydrodynamics," in *Proc. 14th ACM SIGGRAPH/Eurographics Symp. Comput. Animation (SCA)*, Los Angeles, CA, USA, Aug. 2015, pp. 147–155, doi: 10.1145/2786784.2786796.

[17] J. Bender and D. Koschier, "Divergence-free SPH for incompressible and viscous fluids," *IEEE Trans. Vis. Comput. Graphics*, vol. 23, no. 3, pp. 1193–1206, Mar. 2017, doi: 10.1109/TVCG.2016.2578335.

[18] J. Cornelis, J. Bender, C. Gissler, M. Ihmsen, and M. Teschner, "An optimized source term formulation for incompressible SPH," *Vis. Comput.*, vol. 35, no. 4, pp. 579–590, Apr. 2019, doi: 10.1007/s00371-018-1488-8.

[19] M. Macklin, M. Ller, N. Chentanez, and T. Y. and Kim, "Unified particle physics for real-time applications," *ACM Trans. Graph.*, vol. 33, no. 4, p. 153, 2014.

[20] M. Müller, B. Heidelberger, M. Hennix, and J. Ratcliff, "Position based dynamics," *J. Vis. Commun. Image Represent.*, vol. 18, no. 2, pp. 109–118, Apr. 2007, doi: 10.1016/j.jvcir.2007.01.005.

[21] C. Gissler, S. Band, A. Peer, M. Ihmsen, and M. Teschner, "Approximate air-fluid interactions for SPH," in *Proc. 13th Workshop Virtual Real. Interact. Phys. Simulation*, Lyon, France, Apr. 2017, pp. 29–38, doi: 10.2312/vriphys.20171081.

[22] N. Akinci, G. Akinci, and M. Teschner, "Versatile surface tension and adhesion for SPH fluids," *ACM Trans. Graph.*, vol. 32, no. 6, pp. 182:1–182:8, Nov. 2013, doi: 10.1145/2508363.2508395.

[23] H. Schechter and R. Bridson, "Ghost SPH for animating water," *ACM Trans. Graph.*, vol. 31, no. 4, pp. 61:1–61:8, Jul. 2012, doi: 10.1145/2185520.2185557.

[24] T. Liu and Y. Peter Sheng, "Three dimensional simulation of transport and fate of oil spill under wave induced circulation," *Mar. Pollut. Bull.*, vol. 80, nos. 1–2, pp. 148–159, Mar. 2014, doi: 10.1016/j.marpolbul.2014.01.026.

[25] M. Reed, Ø. Johansen, P. J. Brandvik, P. Daling, A. Lewis, R. Fiocco, D. Mackay, and R. Prentki, "Oil spill modeling towards the close of the 20th century: Overview of the state of the art," *Spill Sci. Technol. Bull.*, vol. 5, no. 1, pp. 3–16, Apr. 1999, doi: 10.1016/S1353-2561(98)00029-2.

[26] M. Afenyo, B. Veitch, and F. Khan, "A state-of-the-art review of fate and transport of oil spills in open and ice-covered water," *Ocean Eng.*, vol. 119, pp. 233–248, Jun. 2016, doi: 10.1016/j.oceaneng.2015.10.014.

[27] J. A. Fay, "Physical processes in the spread of oil on a water surface," in *Proc. Int. Oli Spill Conf.*, Washington, DC, USA, Jun. 1971, pp. 463–467, doi: 10.7901/2169-3358-1971-1-463.

[28] W. J. Lehr, H. M. Cekirge, R. J. Fraga, and M. S. Belen, "Empirical studies of the spreading of oil spills," *Oil Petrochem. Pollut.*, vol. 2, no. 1, pp. 7–11, 1984, doi: 10.1016/S0143-7127(84)90637-9.

[29] W. J. Lehr, R. J. Fraga, M. S. Belen, and H. M. Cekirge, "A new technique to estimate initial spill size using a modified fay-type spreading formula," *Mar. Pollut. Bull.*, vol. 15, no. 9, pp. 326–329, Sep. 1984, doi: 10.1016/0025-326X(84)90488-0.

[30] D. P. Hoult, "Oil spreading on the sea," *Annu. Rev. Fluid Mech.*, vol. 4, no. 1, pp. 341–368, Jan. 1972, doi: 10.1146/annurev.fl.04.010172.002013.

[31] O. Johansen, "Doosim—A new simulation model for oil spill management," in *Proc. Int. Oli Spill Conf.*, Washington, DC, USA, Apr. 1987, pp. 529–532, doi: 10.7901/2169-3358-1987-1-529.

[32] F. Ferstl, R. Ando, C. Wojtan, R. Westermann, and N. Thuerey, "Narrow band FLIP for liquid simulations," *Comput. Graph. Forum*, vol. 35, no. 2, pp. 225–232, May 2016, doi: 10.1111/cgf.12825.

[33] T. Sato, C. Wojtan, N. Thuerey, T. Igarashi, and R. Ando, "Extended narrow band FLIP for liquid simulations," *Comput. Graph. Forum*, vol. 37, no. 2, pp. 169–177, May 2018, doi: 10.1111/cgf.13351.

[34] C. J. Zou, "Emergency simulation and visualization of oil spill from ship in navigation simulation," Ph.D. dissertation, Dept. Navig. Coll., Dalian Mar. Univ., Dalian, China, 2018.

[35] W. Si, X. Liao, Y. Qian, Q. Wang, and P.-A. Heng, "Versatile numerical fractures removal for SPH-based free surface liquids," *Comput. Graph.*, vol. 81, pp. 1–8, Jun. 2019, doi: 10.1016/j.cag.2019.03.015.

[36] J. Lee, J.-H. Kim, H.-Y. Lee, and S.-J. Kim, "Realistic fluid representation by anisotropic particle," *J. Visualizat.*, vol. 22, no. 2, pp. 313–320, Apr. 2019, doi: 10.1007/s12650-018-0535-x.

[37] M. Yang, X. Li, Y. Liu, G. Yang, and E. Wu, "A novel surface tension formulation for SPH fluid simulation," *Vis. Comput.*, vol. 33, no. 5, pp. 597–606, May 2017, doi: 10.1007/s00371-016-1274-4.

[38] W. J. van der Laan, S. Green, and M. Sainz, "Screen space fluid rendering with curvature flow," in *Proc. Symp. Interact. 3D Graph. Games (I3D)*, Boston, MA, USA, vol. 1, Feb./Mar. 2009, pp. 91–98, doi: 10.1145/1507149.1507164.

[39] S. Green, "Screen space fluid rendering for games," in *Proc. Games Dev. Conf.*, San Francisco, CA, USA, Mar. 2010, pp. 1–75.

[40] N. N. Truong and C. Yuksel, "A narrow-range filter for screen-space fluid rendering," in *Proc. I3D, ACM SIGGRAPH Symp. Interact. 3D Graph. Games*, Montreal, QC, Canada, May 2018, pp. 17:1–17:15, doi: 10.1145/3203201.

[41] J. Yu and G. Turk, "Reconstructing surfaces of particle-based fluids using anisotropic kernels," *ACM Trans. Graph.*, vol. 32, no. 1, pp. 5:1–5:12, Jan. 2013, doi: 10.1145/2421636.2421641.

[42] M. Müller, D. Charypar, and M. Gross, "Particle-based fluid simulation for interactive applications," in *Proc. ACM SIGGRAPH/Eurographics Symp. Comput. Animation (SCA)*, San Diego, CA, USA, Jul. 2003, pp. 154–159, doi: 10.2312/SCA03/154-159.

[43] J. J. Monaghan, "Smoothed particle hydrodynamics," *Annu. Rev. Astron. Astrophys.*, vol. 30, no. 1, pp. 543–574, Sep. 1992, doi: 10.1146/annurev.aa.30.090192.002551.

[44] M. Ihmsen, J. Orthmann, B. Solenthaler, A. Kolb, and M. Teschner, "SPH fluids in computer graphics," in *Proc. Eurographics-State Art Rep.*, Strasbourg, France, Apr. 2014, pp. 1–22, doi: 10.2312/egst.20141034.

[45] D. Koschier, J. Bender, B. Solenthaler, and M. Teschner, "Smoothed particle hydrodynamics techniques for the physics based simulation of fluids and solids," in *Proc. Eurographics-Tuts.*, Genoa, Italy, May 2019, pp. 1–41, doi: 10.2312/egt.20191035.

[46] J. Bowers, R. Wang, L.-Y. Wei, and D. Maletz, "Parallel Poisson disk sampling with spectrum analysis on surfaces," *ACM Trans. Graph.*, vol. 29, no. 6, pp. 166:1–166:10, Dec. 2010, doi: 10.1145/1882261.1866188.

[47] H. Li, H. Ren, S. Qiu, and C. Wang, "Physics-based simulation of ocean scenes in marine simulator visual system," *Water*, vol. 12, no. 1, pp. 215:1–215:23, Jan. 2020, doi: 10.3390/w12010215.

HAIJIANG LI received the B.E. and M.S. degrees in traffic and transportation engineering from Dalian Maritime University, Dalian, China, in 2013 and 2015, respectively, where he is currently pursuing the Ph.D. degree in traffic information engineering and control with the Key Laboratory of Marine Dynamic Simulation and Control for Ministry of Communications. His research interests are virtual reality, computer graphics, deep learning, and data mining.

HONGXIANG REN received the Ph.D. degree from the Key Laboratory of Marine Simulation and Control for Ministry of Communications, Dalian Maritime University, Dalian, China, in 2009. His research interests include virtual reality, visual simulation, computer vision, computer graphics, and data mining. He is currently a member of the China Image and Graphics Society, the China System Simulation Society, and the China Navigation Society.

CHANG WANG received the B.E. degree in communication engineering from Dalian Jiaotong University, Dalian, China, in 2017, and the M.S. degree in traffic and transportation engineering from the Key Laboratory of Marine Dynamic Simulation and Control for Ministry of Communications, Dalian Maritime University, in 2020. Her research interests are visual simulation and data mining.

SHAOYANG QIU received the B.E. and M.S. degrees in traffic and transportation engineering from Dalian Maritime University, Dalian, China, in 2014 and 2016, respectively, where he is currently pursuing the Ph.D. degree in traffic information engineering and control with the Key Laboratory of Marine Dynamic Simulation and Control for Ministry of Communications. His research interests are virtual reality, visual simulation, and ship motion modeling.